Nanoscale

Spectral attributes of sub-amorphous thermal conductivity in cross-linked organic-inorganic hybrids

Journal:	*Nanoscale*
Manuscript ID	NR-ART-04-2020-002657.R1
Article Type:	Paper
Date Submitted by the Author:	26-May-2020
Complete List of Authors:	Morshedifard, Ali; University of California Irvine Henry Samueli School of Engineering, Civil and Environmental Engineering Moshiri, Amir; University of Houston, Civil and Environmental Engineering Krakowiak, Konrad; University of Houston, Civil and Environmental Engineering Abdolhosseini Qomi, Mohammad Javad; University of California Irvine Henry Samueli School of Engineering,

Nanoscale

ARTICLE TYPE

Cite this: DOI: 00.0000/xxxxxxxxxx

Spectral attributes of sub-amorphous thermal conductivity in cross-linked organic-inorganic hybrids†

Ali Morshedifard,[a] Amir Moshiri,[b] Konrad J. Krakowiak[b], Mohammad Javad Abdolhosseini Qomi*[a]

Received Date
Accepted Date

DOI: 00.0000/xxxxxxxxxx

Organic-inorganic hybrids have found increasing applications for thermal management across various disciplines. Such materials can achieve thermal conductivities below the so-called "amorphous limit" of their constituents' thermal conductivity. Despite their technological significance, a complete understanding of the origins of this thermal conductivity reduction remains elusive in these materials. In this paper, we develop a prototypical cross-linked organic-inorganic layered system, to investigate the spectral origins of its sub-amorphous thermal conductivity. Initially, we study the atomic structure of the model and find that besides polymer chain length, the relative drift of the layers governs the reduction in computed basal spacing, in agreement with experimental measurements. We, subsequently, find that organic cross-linking results in up to 40% reduction in thermal conductivity compared to inorganic samples. An in-depth investigation of vibrational modes reveals that this reduction is the result of reduced mode diffusivities, which in turn is a consequence of a vibrational mismatch between the organic and inorganic constituents. We also show that the contribution of propagating modes to the total thermal conductivity is not affected by organic cross-linking. Our approach paves the path toward a physics-informed analysis and design of a wide range of multifunctional hybrid nanomaterials for thermal management applications among others.

1 Introduction

Organic-inorganic hybrids have found impressively diverse applications in a broad range of industries from electronics to separation technologies.[1] They are used in fuel/solar cells[2], photoelectrochemical water splitting[3], water treatment and separation processes[4], Li-batteries[5], and thermoelectric energy conversion[6] to name just a few (see Mir et al. for a recent review[7]). Recently a broad categorization of such materials has been proposed where organics-in-inorganics hybrids (inorganic materials modified by organic moieties) are distinguished from inorganics-in-organics materials (organic materials or matrices modified by inorganic constituents)[8]. Such hybrid materials can also be tailored for thermal applications for instance in building thermal insulation[9,10], oil wells[11] or pipelines[12,13] in permafrost regions, and thermal barrier coatings[14]. What makes such materials particularly attractive for thermal management is that we can achieve thermal conductivities lower than the amorphous limit[15–17] set by their constituents (e.g., silicates and polymers)[18,19].

Such exotic reduction in thermal conductivities is intimately related to the presence of nanoscale interfaces between dissimilar constituents regardless of whether they have a layered nanostructure or not. For instance, a significant reduction in thermal conductivity of amorphous silicon/germanium superlattices can be achieved due to the Kapitza resistance at the interface between the two constituent layers[20]. Similarly, Au-Si superlattices can also be tailored to achieve ultralow thermal conductivity[21]. Such effects have also been observed when dispersing silicon nanoparticles in polystyrene matrix[22,23].

An important category of hybrid materials that remains less explored (regarding both atomic structure and thermal conductivity) is cross-linked layered organic-inorganic hybrids. Cross-linking inorganic surfaces at the nanoscale remains experimentally challenging[24,25]. Currently, it is achieved by methods such as atomic/molecular layer deposition[26] or electrohydrodynamics[27]. Only recently, covalent cross-linking of calcium-silicate-hydrate layers was achieved using dipodal organosilanes via a sol-gel chemistry technique[28]. Few studies in the literature address thermal conductivity of such materials. Liu et al.[29] measured cross-plane thermal conductivity and volumetric heat capacity for zincone thin films prepared by atomic/molecular layer

[a] Department of Civil and Environmental Engineering, Henry Samueli School of Engineering, E4130 Engineering Gateway, University of California, Irvine, Irvine, CA 92697-2175 USA ; E-mail: mjaq@uci.edu

[b] Civil and Environmental Engineering Department, Cullen College of Engineering, University of Houston, Engineering Building 1, Room N-132, 4726 Calhoun Road, Houston, TX, 77204-4003, USA

† Electronic Supplementary Information (ESI) available.See DOI: 00.0000/00000000.

deposition techniques. Similar results were found by Giri et al. for TiO_2 and ZnO based superlattices with periodic inclusion of organic hydroquinone layers[30]. Losego et al.[31] were also able to utilize a simple self-assembly approach to synthesize organoclay nanocomposites and measure their thermal conductivities using time-domain thermoreflectance. On the atomistic simulation front, recently, Qian et al.[32] developed a force field for organic-inorganic hybrid systems ($\beta-\mathrm{ZnTe(en)_{0.5}}$) and calculated their thermal conductivity using equilibrium molecular dynamics. A common result among such studies is the low/ultra-low thermal conductivities observed in hybrid materials compared to their constituents. Furthermore, the reason for this reduction is commonly attributed to the fact that interfaces impede phonon transport, but a quantitative physics-based clarification of the origins of this reduction seems to be missing. This motivates an in-depth investigation of modal heat transport and characterization of modal vibrations in cross-linked organic-inorganic hybrid materials.

Our objectives in this paper can be stated broadly as: 1- Construction of a model cross-linked organic-inorganic hybrid material and understanding its structural features through free energy calculations. 2- Investigating the impact of organic inclusion on thermal conductivities. 3- Explaining the observed conductivity values through a comprehensive modal analysis. We have chosen 11 Åtobermorite (TB) as our base inorganic material. Dipodal organosilanes with different lengths are grafted to opposing surfaces of TB layers to construct cross-linked organic-inorganic hybrids (XTB). This model only serves as a prototype for this class of layered organic-inorganic hybrids. Using molecular dynamics simulations, we first investigate variations in the basal spacing of hybrid samples with different grafting density and polymer length. Guided by potential-of-mean-force (PMF) calculations, we show that the drift of inorganic layers is the main reason behind the reduction in the basal spacing in hybrid samples at low grafting densities. Next, we use the fluctuation-dissipation theorem-based Green-Kubo approach to calculate the thermal conductivities from equilibrium simulations and show a reduction of up to 40% in heat conductivities in hybrid materials. To further understand the origins of this reduction, a full modal analysis is performed. We use a comprehensive and complementary set of computational techniques to characterize and categorize all vibration modes. We demonstrate that reduced mode diffusivities are the main cause of diminished thermal conductivities in our hybrid system (i.e. cross-linked tobermorite or XTB).

2 Methods

To construct the cross-linked models, we start from the structure of 11 Å tobermorite derived by Hamid[33]. Organosilanes with formulas $(CH_2)_n(SiO_3)_2$ with $n = 2,4,\ldots,12$ are grafted to tobermorite surfaces by substituting two bridging sites with each silicate tetrahedra in the organic molecule. Currently, several force fields are available for modeling inorganic C-S-H (e.g. CSHFF[34,35], CementFF, etc.[36]). Moreover, there are force fields that focus on modeling organic/bio compounds (e.g. CVFF[37] and PCFF[38]). However, due to the presence of organic-inorganic interfaces in our systems, we have chosen the INTERFACE force field[39]. The parameters used in this study are an extension of CVFF for tobermorite minerals. After the model setup, we run molecular dynamics simulations in the NPT ensemble in LAMMPS[40] to equilibrate the system. Nosé-Hoover thermostat and barostat[41] with a time step of 1fs were used for sampling in the NPT ensemble. The basal spacing can be obtained from the ensemble average of the z component of the cell vector. For free energy calculations, we put the same number of organosilanes present in the composite samples on a regular grid. The distance between the center of mass of silica tetrahedra is taken as the collective variable (CV), λ. The potential-of-mean-force (PMF) for this CV is calculated by integrating the mean force, as follows[42]:

$$A(\lambda) = -\int_{\lambda_{min}}^{\lambda} \langle F(x)\rangle \mathrm{d}x \tag{1}$$

The thermal conductivity tensor is computed using the so-called Green-Kubo formalism:

$$\mathbf{K} = \frac{V}{k_B T^2}\int_0^{\infty} \langle \mathbf{J}(0)\otimes\mathbf{J}(t)\rangle \, \mathrm{d}t \tag{2}$$

where $\mathbf{J}$ is the heat flux vector, k_B is the Boltzmann factor, T is temperature and V is the simulation cell volume. See Qomi et al.[43] for more details. Vibrational density of states (VDoS), $g(\omega)$, is computed from the Fourier transform of velocity autocorrelation function as[44]:

$$g(\omega) = \frac{1}{Nk_BT}\sum_{j=1}^{N} m_j \int_{-\infty}^{\infty} \langle \mathbf{v}_j(t)\cdot\mathbf{v}_j(0)\rangle e^{i\omega t}\mathrm{d}t \tag{3}$$

where N is the number of atoms, m_j and $\mathbf{v}_j$ are mass and velocity vector of atom j, respectively.

To study the mode localization, i.e. the spatial extent at which atoms are involved in a given vibrational mode, we calculate the participation ratio[45] for each eigenvector j:

$$P^j = \frac{1}{N\sum_{i=1}^{N}|\varepsilon_i^j|^4} \tag{4}$$

where ε_i^j is the polarization vector of atom i in mode j, while $\sum_{i=1}^{N}|\varepsilon_i^j|^2 = 1$. While the participation ratio of 1 means all atoms participate in a given mode, a P value close to zero means the mode is localized to a small group of atoms[46]. A threshold can be set such that modes with a small P value can be designated as a localized mode.

Characterizing phonon-like propagating modes in amorphous materials is more challenging than detecting localized modes. Usually, the structure factor is employed for this purpose[47]. However, it is not clear how this can be applied in an anisotropic and inhomogeneous setting such as hybrid materials. Recently, an ad-hoc formula has been proposed for computing a quantity called “eigenvector periodicity", which reportedly helps with distinguishing propagons[48]. Here, we propose a method based on a direct discrete Fourier transform of normalized eigenvectors. This is similar, in spirit, to the work of Kaya et al.[49] carried out on disordered colloidal solids. For each vector in the k-space grid (generated compatible with the periodicity of the simulation box

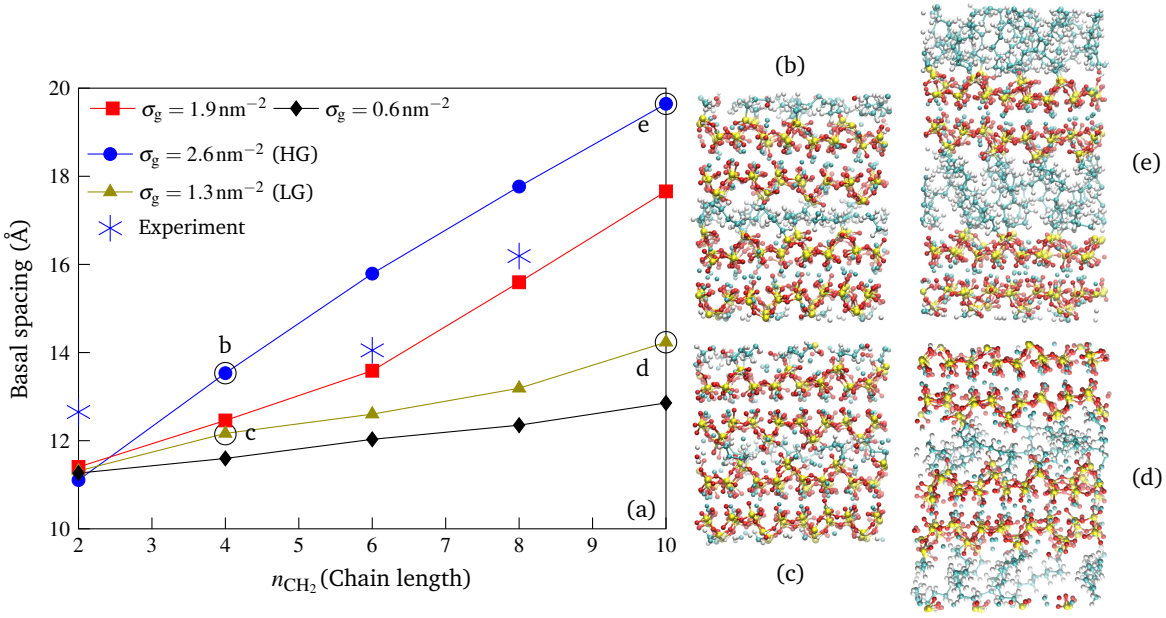

Fig. 1 Structural results after relaxation (a) Variation of basal spacing as a function of grafting percentage and polymer length (Experimental results after Moshiri et al.[28]). (b-e) relaxed structures corresponding to the circled points on the plot.

and interatomic distances), we then have:

$$\gamma^k(\mathbf{k}_r) = |\sum_{j=1}^{N}\sum_{\alpha=1}^{3}\varepsilon^k_{j\alpha}(\mathbf{r}_j)e^{-i\mathbf{k}_r\cdot\mathbf{r}_j}| \tag{5}$$

where $\varepsilon^k_{j\alpha}$ is the α component of polarization vector of atom j and $\mathbf{k}_r$ is rth wavevector in k-space and $\gamma^k(\mathbf{k}_r)$ is the amplitude of sum of Fourier transforms of each component of eigenvector k for wavevector $\mathbf{k}_r$. If a mode has an underlying frequency resembling a $\mathbf{k}_r$ wavevector, $\gamma^k(\mathbf{k}_r)$ will have a large value. In other words, such modes will have at least one outlier within the data set $\{\gamma^k(\mathbf{k}_r) \mid r = 1,2,\ldots,n\}$. To detect if a data set contains such an outlier or not, we use the absolute value of standard score (known as the z-score) commonly used in statistics:

$$z^k_r = \left|\frac{\gamma^k(\mathbf{k}_r) - \mu^k}{\sigma^k}\right| \tag{6}$$

where μ^k and σ^k are the mean and standard deviation of the dataset for mode k. Similar to participation ratio, a threshold can be used to determine if a mode has outliers among amplitudes calculated for various wavevectors and if it does, it can be categorized as a propagon, i.e. phonon-like propagating mode.

Limits of propagon,diffuson and locon regions of the spectrum should be prescribed. Given that locons are determined based on participation ratio (a well-established technique), certain values have been proposed in the literature for the locon-diffuson limit[48]. However, as regards the propagon-diffuson limit, since we are proposing a new technique, a decision has to be made regarding the threshold. Since the final formulation is cast in terms of statistical z-scores, an appropriate value can be adopted considering a probabilistic interpretation. We note that ultimately the categorization is to some extent subjective which is analogous to how the electromagnetic spectrum is divided into segments, namely ultraviolet, X-rays etc.

The last method used in this paper is the formula proposed by Allen and Feldman (AF) for computing mode diffusivities[50]:

$$D_i = \frac{\pi V^2}{3\hbar^2\omega_i^2}\sum_{j}^{\neq i}|S_{ij}|^2\,\delta\left(\omega_i - \omega_j\right) \tag{7}$$

where S is the heat current operator and V is the cell volume and ω_i is the frequency of mode i. From these, we can compute the diffusive thermal conductivity as $\kappa_{\text{diff}} = \frac{1}{V}\sum_i C_i(T)D_i$, where C_i is the heat capacity of mode i. GULP[51] software is used for calculating mode diffusivities in our systems.

3 Results and discussion

The first structural information obtained from our simulations is the basal spacing, as shown in Figure 1. σ_g denotes the number of grafted polymers per surface area and n_{CH_2} denotes the number of CH_2 units in the organosilane polymer (chain length). As expected, the basal spacing increases almost linearly as a function of polymer size[28]. Our recent experimental findings[28] on hybrid systems with a similar structure are compatible with these results as shown in Figure 1. In these experiments, we were able to synthesize hybrid calcium silicate hydrate gels of controlled stoichiometry, and via a sol-gel process using dipodal organosilanes (bis-alkoxysilanes) of alkyl chain lengths (n_{CH_2}) ranging from 2 to 8. The nanostructures were characterized with various techniques including X-ray diffraction (XRD). Presented experimental results, Figure 1, are derived from high-resolution XRD experiments carried out in the low 2θ ($3^\circ \sim 15^\circ$) range, which encompasses the basal reflection of the hybrid systems. More details on synthesis protocols, characterization results and molecular structure can be

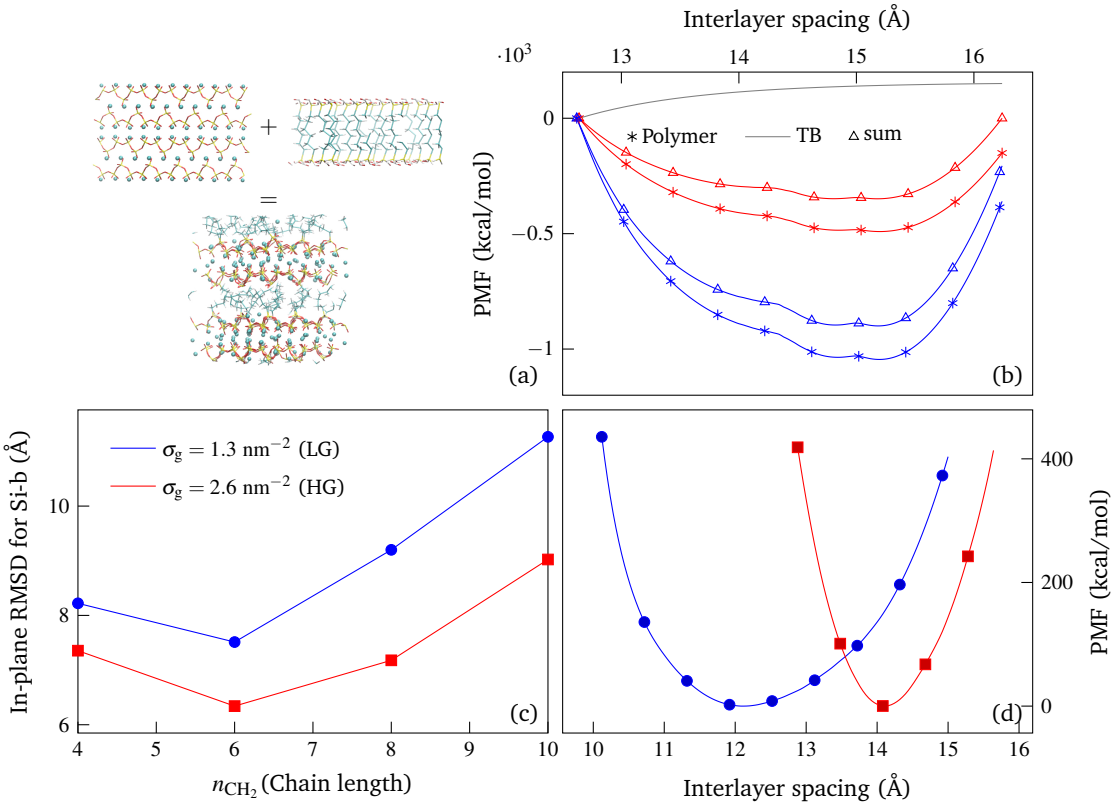

Fig. 2 Leveraging PMF calculations to understand the underlying reasons for observed basal spacing values (a) Potential of mean force (PMF) for $n_{CH_2} = 4$ for high and low grafting (HG and LG respectively) from polymer chains is summed with that of tobermorite (TB). The shift in position of mimima is negligible. The schematic in (b) demonstrate the concept. (c) RMSD for in-plane displacement of grafted bridging silica (Si-b). There is a significantly larger drift for the layers in samples with lower grafting. (d) PMF for real configuration of polymers extracted from relaxed composite structures

found in Moshiri et al[28].

In experiments carried out on clay composites, Losego et al. were also able to control the interlayer spacing by varying chain length and trends similar to those observed in our simulations were obtained[31]. However, experiments are silent on grafting surface densities, σ_g. Figure 1 shows an interesting phenomenon: we have smaller basal spacing at smaller grafting densities for a given polymer length. It is not immediately clear what causes this behavior. We can think of three sources for the reduced basal spacing at a constant n_{CH_2}: **1.** A shift in the equilibrium position of polymers confined between solid layers. This can be verified by investigating the PMF of parallel polymer systems with end-to-end distance as the collective variable. **2.** The dependence of basal stiffness on polymer grafting density and **3.** A layer drift, which causes the polymers to tilt and the interlayer to collapse. What follows is a quantitative investigation of these hypotheses. Due to computational limitations, we only focus on 10 cases: $(\sigma_g, n_{CH_2}) \in \{1.3\text{nm}^{-2}, 2.6\text{nm}^{-2}\} \times \{2,4,6,8,10\}$. Samples with $\sigma_g = 1.3\text{nm}^{-2}$ are labeled LG (low grafting density) and those with $\sigma_g = 2.6\text{nm}^{-2}$ are labeled HG (high grafting density).

First, we construct a regular grid of parallel polymers with the same σ_g as in the composite samples (schematics in Figure 2a). The PMF for these samples with the collective variable being the distance between the layers can be calculated as explained in the methods section. The results for $n_{CH_2} = 4$ and two grafting densities are shown in Figure 2b (other lengths show similar behavior. See Supplementary Information Figure 1S for other cases). Intuitively, when we have higher polymer density, we expect inter-polymer steric repulsion to shift the location of PMF minimum. However, at these values of σ_g, we only see a negligible shift, which means steric repulsion cannot be responsible for the observed decrease in the basal spacing at a constant n_{CH_2}. Moreover, if the PMF from the inorganic part is added to that of the polymer-only system, we still do not see any significant shift in the location of the minimum in the combined organic-inorganic PMF (Figure 2b). This is expected because at such a large basal spacing, the attractive ion correlation forces between the layers are weak[52,53], as seen in the same figure. Also the difference in stiffness values near the minimum ($\partial_\lambda A(\lambda)$) between the two grafting densities is not large enough to cause the observed basal spacing. This means the reduced basal stiffness cannot be at the origins of reduced basal spacing at a given n_{CH_2}.

To investigate the impact of the relative lateral shift between solid layers, we calculate in-plane RMSD of bridging silicons for all samples (Figure 2c). It is clearly seen that there is a significant discrepancy between samples with high and low grafting densities at a constant polymer length. Since layers are cross-linked, the shift results in further tilting of the polymers, which

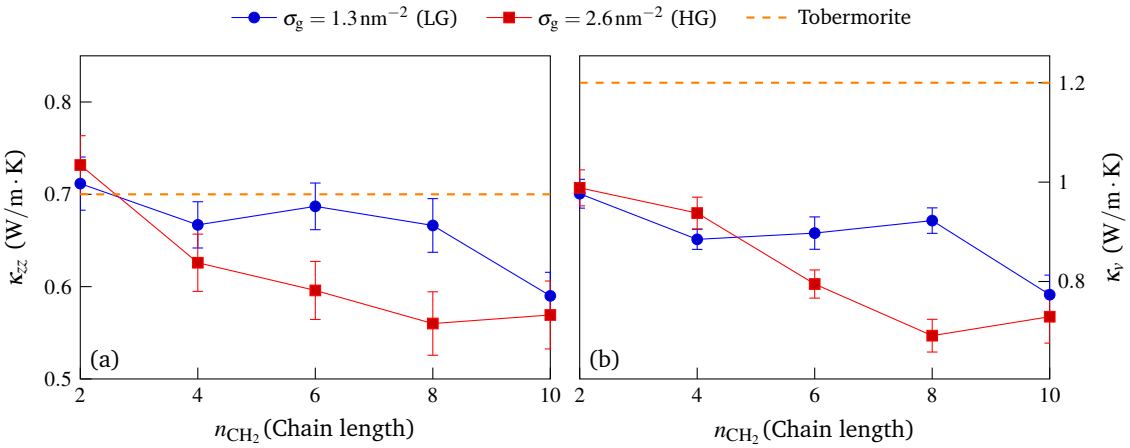

Fig. 3 Reduction in thermal conductivity as longer chains are grafted into the interlayer. (a) cross-plane (z-direction) component of thermal conductivity. (b) Volumetric thermal conductivity. In this case, a significant reduction is observed for even the smallest chain length.

entails a significant collapse of the interlayer spacing. But our simple model of parallel polymers on a regular grid is not able to capture this drift. So, we extract the actual configuration of polymers from the interlayer of relaxed structures and repeat the PMF calculations with these disordered configurations. As shown in Figure 2d, there is a significant shift in the location of PMF minima, which is comparable to values reported earlier in Figure 1. This further confirms that the interlayer drift is the main reason behind the observed reduction in the basal spacing by varying grafting density. A more accurate demonstration would require the addition of sliding collective variables[52], which results in a 3D PMF in the collective variable configuration space. However, this approach currently remains computationally prohibitive.

Once properly relaxed hybrid organic-inorganic atomic structures are at hand, we can compute thermal conductivities using the Green-Kubo (GK) formalism for all samples. Here, we focus on κ_{zz} and the volumetric conductivity $\kappa_v = \frac{\kappa_{xx}+\kappa_{yy}+\kappa_{zz}}{3}$. As can be seen in Figure 3a, for $\sigma_g = 1.3\text{nm}^{-2}$ (LG), we only observe significant reduction in κ_{zz} for the longest chain length ($n_{CH_2} = 10$). For $\sigma_g = 2.6$ nm^{-2} (HG), a steady reduction is observed up to $n_{CH_2} = 8$. There seems to be a plateau after $n_{CH_2} = 8$ which indicates a limit to control the conductivity based on n_{CH_2}. For volumetric conductivity (Figure 3b), we have a reduction in conductivity of about 17% even for $n_{CH_2} = 2$, irrespective of grafting density. $n_{CH_2} = 10$ shows highest reduction for both κ_{zz} and κ_v (17% and 40%, respectively). We now focus on understanding the origins of the observed reduction in thermal conductivity.

As a first attempt, one might model thermal conductivity using a simple series model such as the following:

$$\frac{d_{\text{total}}}{\kappa_{\text{eff}}} = \sum_{\text{layers}} \frac{d_i}{\kappa_i} + \sum_{\text{interfaces}} \frac{1}{G_i} \tag{8}$$

where d is layer thickness and G is the interfacial thermal conductance. For TB layers, we assume $\kappa_{TB} = 1.2$ W/m·K and $d_{TB} = 11.2$ Å. For the organic layer, we take $\kappa_{ORG} = 0.15$ W/m·K in our approximation based on values reported in the literature for amorphous polymers ($0.1 \sim 0.2$ W/m·K)[54]. Neglecting interface contributions, for (HG)$n_{CH_2} = 6, 8$ we get $\kappa_{\text{eff}} = 0.39, 0.33$ W/m·K, respectively, which is significantly lower than our GK calculations. Several contributing factors can be cited for the observed discrepancy. First, we expect the short polymer chains in our study, which are also covalently bonded to inorganic layers to have higher conductivity than bulk conductivity of amorphous polymers[55]. This is supported by previous investigations on the effect of bonding and cross-linking on thermal conductivity[56,57]. Moreover, we used the bulk value of conductivity for the tobermorite layer, while the conductivity of a single layer is unknown. Bulk values can be further corrected due to size effects when they are used in continuum calculations[58], which further reduces κ_{TB} in Equation 8. The result is further reduction of κ_{eff} and further deviation from atomistic results. There are also interface effects between TB layers which is unknown when doing bulk calculations. The above discussion underlines the fact that simple continuum models are inadequate for our complex system at such small scales and more holistic modal analysis approaches are required to better understand the underlying physics of heat transport in organic-inorganic hybrids.

Figure 4 (a) shows vibrational density of states for TB, XTB at $n_{ch2} = 8$ with high grafting (HG) and that of a single polymer. In a frequency range of 30∼45 THz, we can see that polymer molecules have modes that are absent in TB. Hence, we can expect this modal mismatch to result in scattering at the interface between TB and the organic material, which manifests as reduced diffusivities as we show later on. In the literature, this vibrational mismatch is cited as the underlying reason for lower conductivity[20,32]. This hypothesis can be further investigated by a full characterization of vibrational modes of the systems. Based on their spatial vector fields, these modes can be categorized into locons, diffusons or propagons[50]. To distinguish locons, we compute the modal participation ratio (PR) for all modes of each sample (a typical result is shown in Figure 4b). As discussed in the methods section, a cutoff value is needed (e.g. a value of 0.1 as used in some previous studies[48]). In this study, we use a more conservative value and modes with a PR smaller than 0.05 are labeled as locons. Note that a higher value would result in higher con-

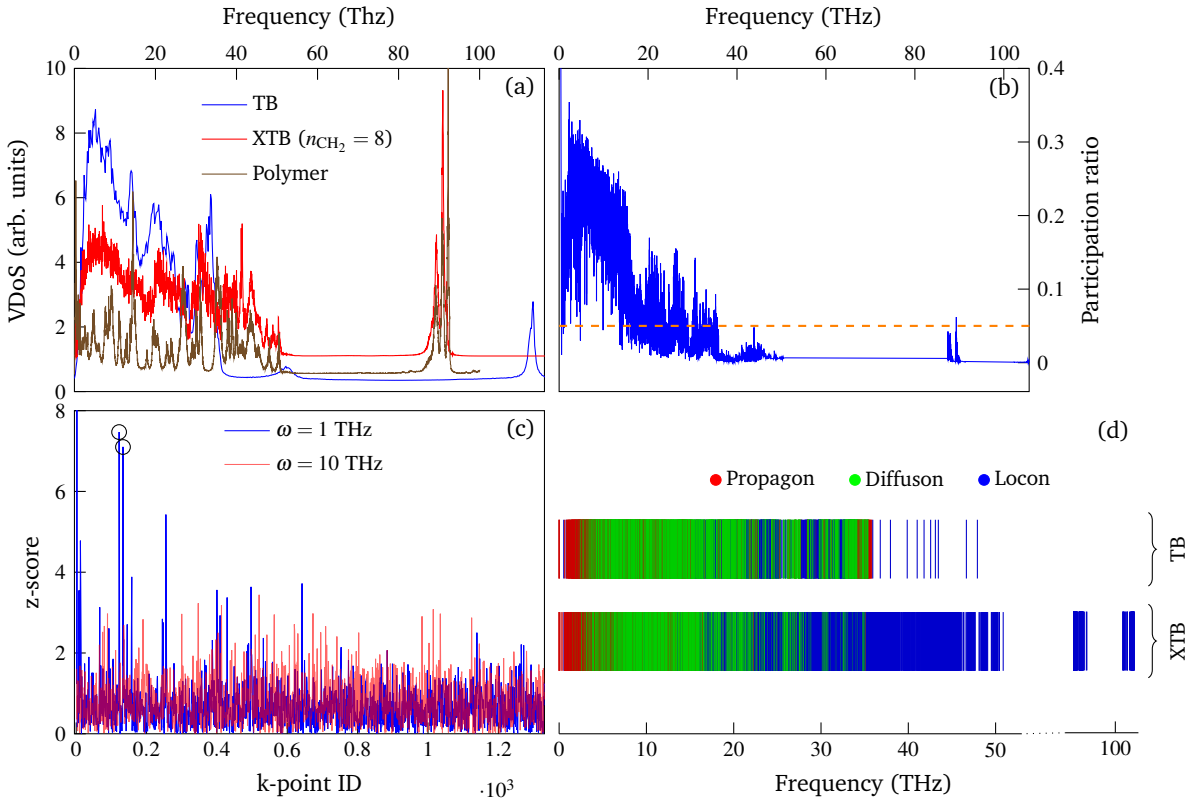

Fig. 4 Modal analysis for tobermorite and cross-linked tobermorite (XTB) with $n_{CH_2} = 8$. (a) Vibrational density of states for tobermorite, polymer and XTB with $n_{CH_2} = 8$. Adding organic constituents introduces modes in an interval of about 30∼50 THz which is absent in tobermorite. This results in a vibrational mismatch between the organic and inorganic layers and leads to reduced mode diffusivities (b) Participation ratios are calculated for each mode. This data is used to distinguish locons (c) Results for spatial Fourier decomposition of two typical modes on the 3D Fourier basis. At lower frequencies, modes show dominant (outlier) amplitudes for particular wavevectors and are designated as propagons. The rest (except those already designated as locons) are labeled as diffusons (d) Full modal spectrum for TB and XTB with $n_{CH_2} = 8$. We can visually see the abundance of localized modes in the hybrid case compared to pristine tobermorite.

ductivities. Moreover, the calculations are not sensitive to this limit since higher frequency modes (whose inclusion or exclusion is affected by the limit) already have small contributions to conductivity.

To distinguish propagating modes, we use equation 5 as described in the methods section. The results for two modes with low and medium frequencies are shown in Figure 4c. We see that modes with lower frequency (1 THz here) show marked peaks, which are absent from modes with higher frequency (10 THz here). Regarding threshold value, as in the diffuson-locon limit, we choose a very conservative value of 6 for detecting propagons. This means that we have an outlier if the frequency amplitude has a negligible probability. In other words, we should have one or more sharp spikes in the data as in Figure 4c. After distinguishing localized and propagating modes, the remaining modes are labeled as diffusons. Figure 4d shows the full characterization spectrum for both TB and XTB. For TB, we calculated vibrational modes after introducing a defect in the system. However, due to crystallinity, a few anomalous propagating modes are observed at higher frequencies. Our results are compatible with previous findings for amorphous silicon, where propagating modes were observed even beyond the Ioffe-Regel threshold[48,59]. From this spectrum, we can see that although a sharp difference is observed in the number of locons for TB and XTB, both have more or less the same number of propagons. But why do we have such a stark difference in the percentage of locons between TB and the composite system?

In Figure 5, we plot the number of locons and propagons as a function of degrees of freedom (DoFs) that are added to the TB structure (all added DoFs belong to the organic part). Interestingly, we find that locons increase with a slope of almost 1, while the number of propagons shows a negligible increase. This is what was visually observed in Figure 4d as well. In a sense, one could say that although the number of modes available for thermal transport is more numerous in the hybrid system, those added DoFs are all localized and do not contribute to heat transport. So one can conclude that it is a change in the character of the same number of either diffusons or propagons that is lowering the thermal conductivity of the hybrid material.

To investigate this hypothesis quantitatively, we try to separate the diffusive part of conductivity (κ_ν^d) from the propagative part (κ_ν^p). This can be done by computing κ_ν^d using Allen-Feldman theory as described in the methods section, which gives $\kappa_\nu^p = \kappa_\nu - \kappa_\nu^d$. Figure 6a shows that κ_ν^d remarkably has the same decreasing trend as the total conductivity shown in Figure 3 and constitutes roughly 33∼50% of κ_ν. This value can be contrasted

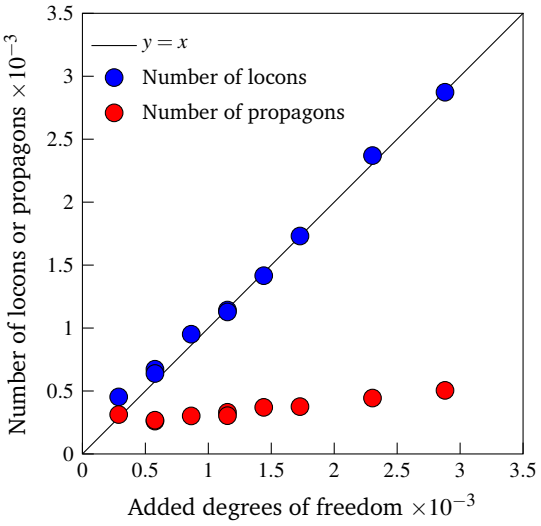

Fig. 5 Number of locons and propagons in each sample as a function of added degrees of freedom. For locons, a linear relationship with a slope of 1 is observed which indicates modes added due to polymers are all locons. However, the number of propagons shows a negligible increase.

with the higher diffusive contribution in a more disordered system obtained by Zhou et al.[60]. However, as seen from Figure 6b, such trend is non-existent for $\kappa_\nu^p = \kappa_\nu - \kappa_\nu^d$. This points to the fact that the reduction in thermal conductivity mainly arises from a change in mode diffusivities. In the literature, this reduction is routinely attributed to "scattering of phonons at the interface" with the implicit assumption that the propagating modes are the only contributor. This is justifiable for multilayered crystalline materials with sharp interfaces (e.g. thermal interface conductance in Si/Ge superlattices[61]) studied in the literature. However, in our case the results show that the propagon contribution remains unchanged due to cross-linking and the reduction can only be attributed to diffusons. It further underlines the importance of full spectral analysis in complex hybrid materials.

Figure 6c shows mode diffusivities for a number of cross-linked models ($n_{CH_2} = 2$ (LG), $n_{CH_2} = 10$ (LG), $n_{CH_2} = 2$ (HG), $n_{CH_2} = 10$ (HG)) and the pristine TB. We see that overall, models with larger polymer length and higher grafting show lower diffusivities. These diffusivities can be used to compute cumulative κ_ν^d for each model which is shown in Figure 6d. Therein, we clearly see the reduced cumulative κ_ν^d which arises as a result of hampered diffusivities. Combined with unchanged contribution from propagating modes, this quantitatively demonstrates that the reduction in heat conductivity can only be due to the reduced mode diffusivity of diffusons, which is in turn rooted in the modified interfaces in cross-linked samples compared to the pristine inorganic structure.

The procedures discussed in this paper for separating propagating and diffusive contributions to thermal conductivity can just as well be applied to a range of materials (including materials with nanoconfined water[62]) to better understand the mechanisms underlying their heat transport. Such fundamental knowledge would ultimately assist with the design of new nanomaterials and nanoscale thermal processes. For instance, an interface is created when a nanoparticle is embossed through laser heating in a polymer matrix[63] which is amenable to a spectral analysis. Moreover, metal organic frameworks (MOFs) are a primary choice for water uptake at low relative humidity[64], as in design of energy efficient adsorption-based chillers[65].

It might be challenging to find biological applications for the particular prototype material used in our study. However, there are biological/biomimetic materials with similar characteristics amenable to thermal analysis. For instance, nacre is composed of platelets of aragonite separated by sheets of an organic matrix. Artificial analogs of nacre[66] can be synthesized with nanoscale platelet sizes which makes them ideal multifunctional materials where high fracture toughness and low thermal conductivity are simultaneously desired. In addition to nacre, layered double hydroxides (such as clays), which have similar structures to our system, can be used as controlled release systems for pesticides, genes and drugs among others[67]. Our experimental findings[28] show negligible swelling/shrinkage in these materials which can enhance the release of nanoconfined fluids without interlayer collapse. Chitosan-silane hybrids are another important class of materials which find applications in membranes, tissues or scaffolds[68].

Conclusions

The following concluding remarks summarize the new findings presented in this paper:

1. Bipodal organosilanes with different chain lengths can be used to cross-link nanoscale interfaces of layered inorganic materials such as tobermorite and phyllosilicates with different surface grafting densities. Higher grafting means larger basal spacing (at a constant polymer chain length) and in this paper, we have shown that the drift in the inorganic layer lies at the origins of this difference.

2. We show that organic cross-linking can reduce volumetric thermal conductivity as much as 40%, which is lower than values obtainable from pristine amorphous inorganic components.

3. A simple method for characterizing propagons was introduced. We show that the number of propagons is more or less unchanged as a function of carbon content. We also show, using participation ratio that the added organic modes due to cross-linking are all localized in nature.

4. By computing mode diffusivities for all modes of all samples, we show that a reduction in mode diffusivities in cross-linked systems is the main cause of the lower thermal conductivities observed in our organic-inorganic composites.

We envision that these findings can potentially pave the path toward designing a new generation of low-thermal conductivity insulating materials, which is the subject of our ongoing investigations. It is conceivable that our findings can have direct implications for designing thermally insulating hybrid materials with applications ranging from automotive to space industries.

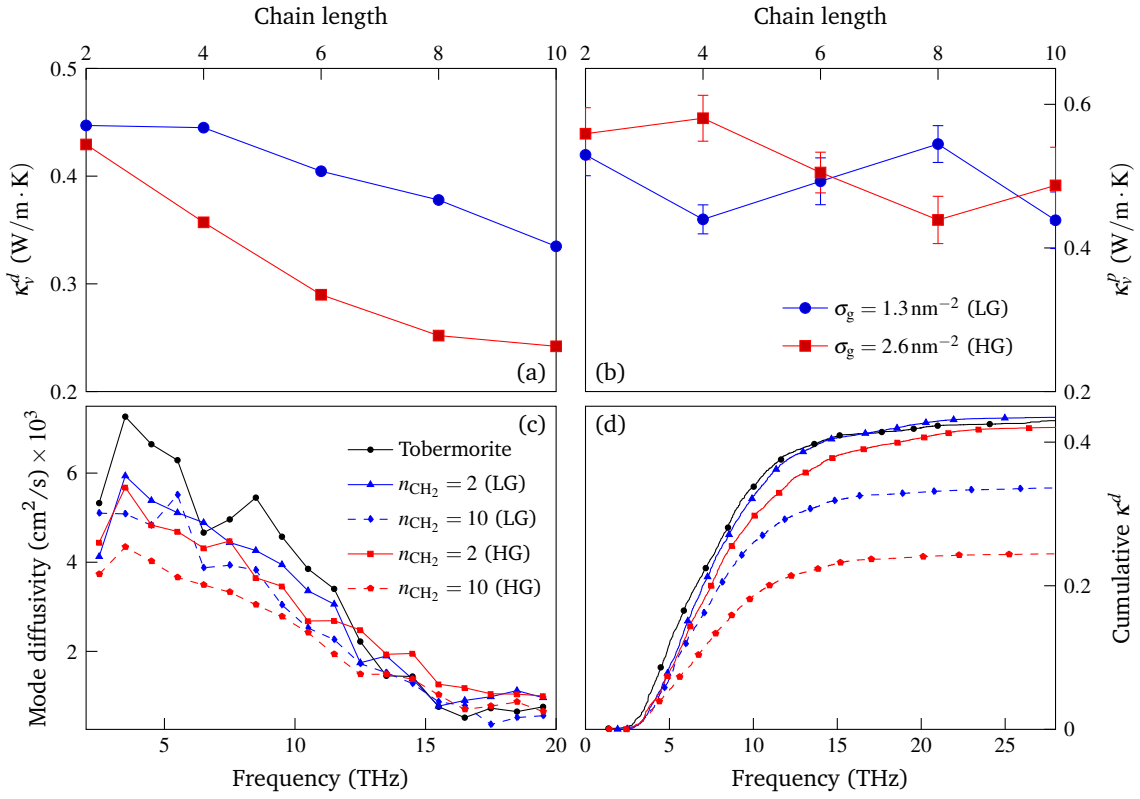

Fig. 6 Decomposition of thermal conductivity into propagating and diffusive components and understanding origins of observed differences in diffusive contribution to thermal conductivity (a) The diffusive component computed using Allen-Feldman theory. The trend is similar to what was computed using Green-Kubo in this paper. (b) Propagon contribution obtained as $\kappa_\nu^p = \kappa_\nu - \kappa_\nu^d$. We see that the decreasong trend disappears. (c) Comparison of mode diffusivities for a number of cross-linked models and pristine TB. Overall, mode diffusivities show significant reduction due to cross-linking, where we have high grafting and long chain lengths. (d) Cumulative diffusive contribution to the thermal conductivity. For small chain length and low grafting percentage, we do not observe a significant change in κ^d compared to the pristine TB. The reduction is most significant for large chain lengths and high grafting percentages. See Figure 2S in Supplementary materials for other grafting and chain lengths. Lines in figures are guides for the eye.

From a computational prospective, this work opens up paths for future research. At larger scales, the building blocks of the hybrid material studied (similar to pristine tobermorite) can be modeled as globules of several cross-linked layers. A coarse-grained model can be developed through free energy calculations and judicious choice of interaction potentials among these particles[69]. Once the meso-texture is at hand, upscaling of material properties can be achieved. Since we have already calculated thermal conductivity for the hybrid material at the nanoscale, a homogenization technique such as Mori-Tanaka theory can be used to compute conductivities at larger scales[70] based on computed porosities. Density, pore-size distribution and creep performance[71] are among other properties that can be studied using mesoscale models.

Acknowledgements

This work was supported by the National Science Foundation under Grants No. 1825921 and 1826122. We thank Dr. Ratan K. Mishra, Tariq Jamil and Professor Hendrik Heinz for providing us with the INTERFACE force field for cementitious materials.

Notes and references

1 C. Sanchez, B. Julián, P. Belleville and M. Popall, *Journal of Materials Chemistry*, 2005, **15**, 3559–3592.
2 C. Laberty-Robert, K. Valle, F. Pereira and C. Sanchez, *Chemical Society Reviews*, 2011, **40**, 961–1005.
3 F. Fumagalli, S. Bellani, M. Schreier, S. Leonardi, H. C. Rojas, A. Ghadirzadeh, G. Tullii, A. Savoini, G. Marra, L. Meda *et al.*, *Journal of Materials Chemistry A*, 2016, **4**, 2178–2187.
4 S.-L. Wu, F. Liu, H.-C. Yang and S. B. Darling, *Molecular Systems Design & Engineering*, 2020.
5 J. Shim, D.-G. Kim, J. H. Lee, J. H. Baik and J.-C. Lee, *Polymer Chemistry*, 2014, **5**, 3432–3442.
6 A. Minnich, M. S. Dresselhaus, Z. Ren and G. Chen, *Energy & Environmental Science*, 2009, **2**, 466–479.
7 S. H. Mir, L. A. Nagahara, T. Thundat, P. Mokarian-Tabari, H. Furukawa and A. Khosla, *Journal of The Electrochemical Society*, 2018, **165**, B3137–B3156.
8 A. G. Skirtach, M. S. Saveleva, K. Eftekhari, A. Abalymov, T. E. Douglas, D. Volodkin and B. V. Parakhonskiy, *Frontiers in chemistry*, 2019, **7**, 179.
9 B. P. Jelle, A. Gustavsen and R. Baetens, *Journal of Building*

Physics, 2010, **34**, 99–123.
10 K. J. Krakowiak, R. G. Nannapaneni, A. Moshiri, T. Phatak, D. Stefaniuk, L. Sadowski and M. J. A. Qomi, *Cement and Concrete Composites*, 2020, 103514.
11 J. W. Hyde and W. J. George, *Oil well and method for production of oil through permafrost zone*, 1971, US Patent 3,613,792.
12 J. Zhang, G. Qu and H. Jin, *Cold regions science and technology*, 2010, **64**, 243–247.
13 A. Bahadori, *Thermal insulation handbook for the oil, gas, and petrochemical industries*, Gulf Professional Publishing, 2014.
14 D. R. Clarke and S. R. Phillpot, *Materials today*, 2005, **8**, 22–29.
15 D. G. Cahill and R. Pohl, *Solid State Communications*, 1989, **70**, 927–930.
16 N. Burger, A. Laachachi, M. Ferriol, M. Lutz, V. Toniazzo and D. Ruch, *Progress in Polymer Science*, 2016, **61**, 1–28.
17 H. Mizuno, S. Mossa and J.-L. Barrat, *Scientific reports*, 2015, **5**, 14116.
18 J. M. Larkin and A. J. McGaughey, *Physical Review B*, 2014, **89**, 144303.
19 F. DeAngelis, M. G. Muraleedharan, J. Moon, H. R. Seyf, A. J. Minnich, A. J. McGaughey and A. Henry, *Nanoscale and Microscale Thermophysical Engineering*, 2019, **23**, 81–116.
20 A. Giri, P. E. Hopkins, J. G. Wessel and J. C. Duda, *Journal of Applied Physics*, 2015, **118**, 165303.
21 E. Dechaumphai, D. Lu, J. J. Kan, J. Moon, E. E. Fullerton, Z. Liu and R. Chen, *Nano letters*, 2014, **14**, 2448–2455.
22 F. B. Juangsa, Y. Muroya, M. Ryu, J. Morikawa and T. Nozaki, *Applied Physics Letters*, 2017, **110**, 253105.
23 A. Tlili, V. Giordano, Y. Beltukov, P. Desmarchelier, S. Merabia and A. Tanguy, *Nanoscale*, 2019, **11**, 21502–21512.
24 H. Matsuyama and J. F. Young, *Chemistry of materials*, 1999, **11**, 16–19.
25 J. Minet, S. Abramson, B. Bresson, C. Sanchez, V. Montouillout and N. Lequeux, *Chemistry of materials*, 2004, **16**, 3955–3962.
26 X. Qian, X. Gu and R. Yang, *Nano Energy*, 2017, **41**, 394–407.
27 W. J. Thrift, C. Q. Nguyen, M. Darvishzadeh-Varcheie, S. Zare, N. Sharac, R. N. Sanderson, T. J. Dupper, A. I. Hochbaum, F. Capolino, M. J. Abdolhosseini Qomi *et al.*, *ACS nano*, 2017, **11**, 11317–11329.
28 A. Moshiri, D. Stefaniuk, S. K. Smith, A. Morshedifard, D. F. Rodrigues, M. J. A. Qomi and K. J. Krakowiak, *Cement and Concrete Research*, 2020, **133**, 106076.
29 J. Liu, B. Yoon, E. Kuhlmann, M. Tian, J. Zhu, S. M. George, Y.-C. Lee and R. Yang, *Nano letters*, 2013, **13**, 5594–5599.
30 A. Giri, J.-P. Niemelä, C. J. Szwejkowski, M. Karppinen and P. E. Hopkins, *Physical Review B*, 2016, **93**, 024201.
31 M. D. Losego, I. P. Blitz, R. A. Vaia, D. G. Cahill and P. V. Braun, *Nano letters*, 2013, **13**, 2215–2219.
32 X. Qian, X. Gu and R. Yang, *The Journal of Physical Chemistry C*, 2015, **119**, 28300–28308.
33 S. Hamid, *Zeitschrift für Kristallographie-Crystalline Materials*, 1981, **154**, 189–198.
34 R. Shahsavari, R. J.-M. Pellenq and F.-J. Ulm, *Physical Chemistry Chemical Physics*, 2011, **13**, 1002–1011.
35 P. J. Monteiro, G. Geng, D. Marchon, J. Li, P. Alapati, K. E. Kurtis and M. J. A. Qomi, *Cement and Concrete Research*, 2019, **124**, 105806.
36 R. K. Mishra, A. K. Mohamed, D. Geissbühler, H. Manzano, T. Jamil, R. Shahsavari, A. G. Kalinichev, S. Galmarini, L. Tao, H. Heinz *et al.*, *Cement and Concrete Research*, 2017, **102**, 68–89.
37 P. Dauber-Osguthorpe, V. A. Roberts, D. J. Osguthorpe, J. Wolff, M. Genest and A. T. Hagler, *Proteins: Structure, Function, and Bioinformatics*, 1988, **4**, 31–47.
38 J. Blomqvist, L. Ahjopalo, B. Mannfors and L.-O. Pietilä, *Journal of Molecular Structure: THEOCHEM*, 1999, **488**, 247–262.
39 H. Heinz, T.-J. Lin, R. Kishore Mishra and F. S. Emami, *Langmuir*, 2013, **29**, 1754–1765.
40 S. Plimpton, *Fast parallel algorithms for short-range molecular dynamics*, Sandia national labs., albuquerque, nm (united states) technical report, 1993.
41 S. Rogge, L. Vanduyfhuys, A. Ghysels, M. Waroquier, T. Verstraelen, G. Maurin and V. Van Speybroeck, *Journal of chemical theory and computation*, 2015, **11**, 5583–5597.
42 G. Munaò, A. Pizzirusso, A. Kalogirou, A. De Nicola, T. Kawakatsu, F. Müller-Plathe and G. Milano, *Nanoscale*, 2018, **10**, 21656–21670.
43 M. J. A. Qomi, F.-J. Ulm and R. J.-M. Pellenq, *Physical Review Applied*, 2015, **3**, 064010.
44 B. T. Wong and P. M. Mengüç, *Thermal transport for applications in micro/nanomachining*, Springer Science & Business Media, 2008.
45 R. Bell and P. Dean, *Discussions of the Faraday society*, 1970, **50**, 55–61.
46 T. Zhu and E. Ertekin, *Nano letters*, 2016, **16**, 4763–4772.
47 J. L. Feldman, P. B. Allen and S. R. Bickham, *Physical Review B*, 1999, **59**, 3551.
48 H. R. Seyf and A. Henry, *Journal of Applied Physics*, 2016, **120**, 025101.
49 D. Kaya, N. Green, C. Maloney and M. Islam, *Science*, 2010, **329**, 656–658.
50 P. B. Allen and J. L. Feldman, *Physical Review B*, 1993, **48**, 12581.
51 J. D. Gale, *Journal of the Chemical Society, Faraday Transactions*, 1997, **93**, 629–637.
52 S. Masoumi, H. Valipour and M. J. Abdolhosseini Qomi, *The Journal of Physical Chemistry C*, 2017, **121**, 5565–5572.
53 S. Masoumi, S. Zare, H. Valipour and M. J. Abdolhosseini Qomi, *The Journal of Physical Chemistry C*, 2019, **123**, 4755–4766.
54 X. Wei and T. Luo, *Physical Chemistry Chemical Physics*, 2019, **21**, 15523–15530.
55 S. Shen, A. Henry, J. Tong, R. Zheng and G. Chen, *Nature nanotechnology*, 2010, **5**, 251.
56 G.-H. Kim, D. Lee, A. Shanker, L. Shao, M. S. Kwon, D. Gidley,

J. Kim and K. P. Pipe, *Nature materials*, 2015, **14**, 295–300.
57 M. D. Losego, M. E. Grady, N. R. Sottos, D. G. Cahill and P. V. Braun, *Nature materials*, 2012, **11**, 502–506.
58 G. Chen, 1997.
59 J. Moon, B. Latour and A. J. Minnich, *Physical Review B*, 2018, **97**, 024201.
60 Y. Zhou, A. Morshedifard, J. Lee and M. J. Abdolhosseini Qomi, *Applied Physics Letters*, 2017, **110**, 043104.
61 Y. Chalopin, K. Esfarjani, A. Henry, S. Volz and G. Chen, *Physical Review B*, 2012, **85**, 195302.
62 M. J. A. Qomi, M. Bauchy, F.-J. Ulm and R. J.-M. Pellenq, *The Journal of chemical physics*, 2014, **140**, 054515.
63 A. G. Skirtach, D. G. Kurth and H. Möhwald, *Applied Physics Letters*, 2009, **94**, 093106.
64 A. Cadiau, J. S. Lee, D. Damasceno Borges, P. Fabry, T. Devic, M. T. Wharmby, C. Martineau, D. Foucher, F. Taulelle, C.-H. Jun *et al.*, *Advanced Materials*, 2015, **27**, 4775–4780.
65 D. Lenzen, P. Bendix, H. Reinsch, D. Fröhlich, H. Kummer, M. Möllers, P. P. Hügenell, R. Gläser, S. Henninger and N. Stock, *Advanced Materials*, 2018, **30**, 1705869.
66 Z. Tang, N. A. Kotov, S. Magonov and B. Ozturk, *Nature materials*, 2003, **2**, 413–418.
67 P. Saikia, A. Borah, R. L. Goswamee *et al.*, *Colloid and Polymer Science*, 2017, **295**, 725–747.
68 S. Spirk, G. Findenig, A. Doliska, V. E. Reichel, N. L. Swanson, R. Kargl, V. Ribitsch and K. Stana-Kleinschek, *Carbohydrate polymers*, 2013, **93**, 285–290.
69 S. Masoumi, D. Ebrahimi, H. Valipour and M. J. Abdolhosseini Qomi, *Journal of the American Ceramic Society*, 2020, **103**, 541–557.
70 H. J. Böhm and S. Nogales, *Composites Science and Technology*, 2008, **68**, 1181–1187.
71 A. Morshedifard, S. Masoumi and M. A. Qomi, *Nature communications*, 2018, **9**, 1–10.

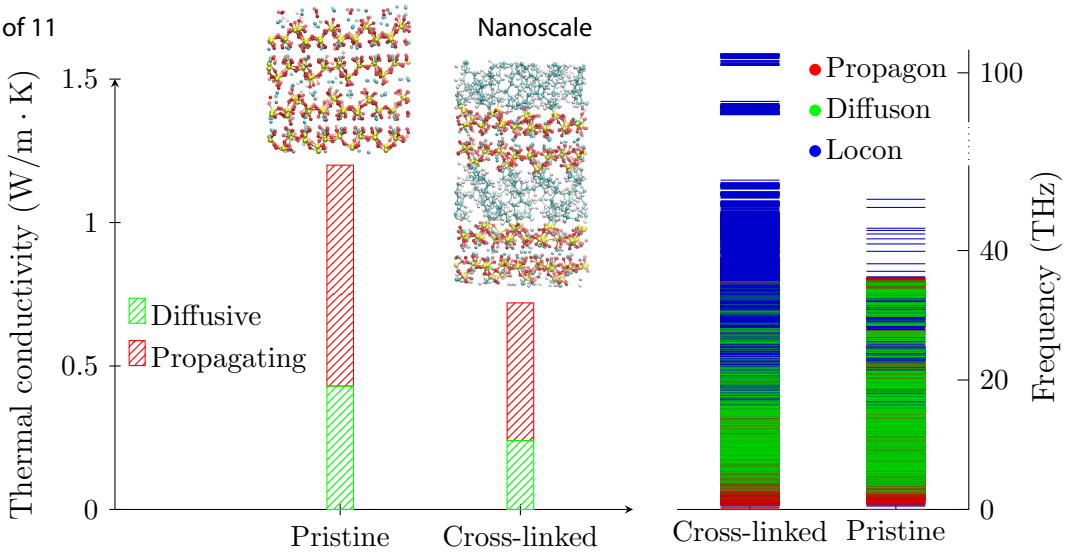

Comparison of thermal conductivity in hybrid materials and pristine inorganic samples and the modal spectrum of each sample showing approximately unchanged number of propagating modes and significant number of added localized modes in the hybrid sample.